catalysts

MDPI

Article

Peroxymonosulfate Activation by CuO-Fe_2O_3-Modified Ni Foam: A $^1O_2$ Dominated Process for Efficient and Stable Degradation of Tetracycline

Xueqing Ren [1], Peng Xu [2,*], Ke Tian [1], Menghan Cao [1], Fengyin Shi [1] and Guangshan Zhang [1,*]

[1] College of Resource and Environment, Qingdao Engineering Research Center for Rural Environment, Qingdao Agricultural University, Qingdao 266109, China
[2] State Key Laboratory of Urban Water Resource and Environment, School of Environment, Harbin Institute of Technology, Harbin 150090, China
* Correspondence: 18636284364@163.com (P.X.); gszhang@qau.edu.cn (G.Z.); Tel./Fax: +86-1556-1566-038 (P.X.); +86-532-5895-7461 (G.Z.)

Abstract: The post-separation of powder catalysts restricts the practical application of peroxymonosulfate (PMS)-based advanced oxidation technology. Hence, we fabricated CuO-Fe_2O_3-modified Ni foam (CFO-NF) using a facile hydrothermal method for an efficient PMS activation. The CFO-NF/PMS system could achieve a 97.9% tetracycline hydrochloride (TC) removal efficiency in 60 min with four pieces of CFO-NF and 0.4 mmol L^{-1} of PMS. The removal efficiency was maintained at >85% even after five cycles, indicating the excellent stability of CFO-NF composites. The conversion among Fe(III)/Fe(II), Cu(II)/Cu(I), and Ni(III)/Ni(II) accelerated the PMS decomposition, verifying the synergy between CuO-Fe_2O_3 and Ni foam. The trapping experiments and EPR detection confirmed that abundant active species (•OH, $SO_4^{\bullet-}$, $O_2^{\bullet-}$, and $^1O_2$) were produced in the CFO-NF/PMS system, accounting for the existence of radical pathways and a non-radical pathway, in which $^1O_2$ (non-radical pathway) was dominated. This study developed a novel CuO-Fe_2O_3-modified Ni foam with a superior PMS activation performance, a high stability, and a recoverability for eliminating refractory organic pollutants.

Keywords: CuO-Fe_2O_3-modified Ni foam; peroxymonosulfate; tetracycline; stability; singlet oxygen

Citation: Ren, X.; Xu, P.; Tian, K.; Cao, M.; Shi, F.; Zhang, G. Peroxymonosulfate Activation by CuO-Fe_2O_3-Modified Ni Foam: A $^1O_2$ Dominated Process for Efficient and Stable Degradation of Tetracycline. *Catalysts* **2023**, *13*, 329. https://doi.org/10.3390/catal13020329

Academic Editor: Leonarda Liotta

Received: 2 February 2022
Revised: 13 January 2023
Accepted: 20 January 2023
Published: 2 February 2023

1. Introduction

Antibiotics have been widely used to guarantee human safety, animal husbandry, and agricultural production [1]. The extensive use of tetracycline (TC), a typical broad-spectrum antibiotic, is inevitably discharged into the natural environment due to an incomplete metabolism [2]. The exposure of TC to the environment seriously threatens human health and other organisms due to its high chemical stability (a half-life of ~34–329 h) and water solubility, carcinogenicity, low biodegradability, and apparent ecological toxicity [3]. Hence, developing an effective technology for TC degradation is crucial and urgent.

To address this challenge, peroxymonosulfate (PMS)-based advanced oxidation technology is an appropriate choice due to its superior oxidizing ability and adaptability in the degradation of organic pollutants. Compared with •OH, $SO_4^{\bullet-}$ produced from PMS possesses a higher oxidation potential (2.5–3.1 V vs. NHE), longer half-life (30–40 µs), and broader operating in the pH range, which are beneficial to the degradation process [4,5]. Various PMS activation methods, such as heat, alkali, ultrasound, ultraviolet light, carbonaceous materials, etc. [6–9], have been explored to produce active species. Among these, transition metal-based catalysts are regarded as a suitable candidate for efficiently triggering PMS, with which cobalt-based catalysts were the best [10–12]. However, the toxicity and environmental risk cannot be ignored. To this end, eco-friendly cobalt-free catalysts, such as ones which are iron-based, copper-based, etc., are developed to activate

PMS. Furthermore, the higher performance of polymetallic catalysts for the activation of PMS compared to monometallic catalysts is attributed to the synergistic effect through a valence conversion between multiple metals [13]. Therefore, we fabricate a CuO-Fe_2O_3 bimetallic oxide catalyst to activate PMS efficiently.

Despite the better catalytic performance of CuO-Fe_2O_3, the post-separation of powder catalysts is always a complex and time-consuming recovery process restricting its practical application. In addition, the leakage of powder catalysts harms human health and the natural environment. One feasible approach is immobilizing powder materials on substrate materials [14,15]. Nickel foam (NF) has been widely used as an ideal supporter due to its excellent mechanical and thermal stability, large surface area, high porosity, and interconnected 3D framework [16]. The NF backbones can also provide channels for the charge transport to enhance the catalytic performance [17]. Moreover, metallic nickel in NF might also play a synergistic role in the PMSs activation through valence conversion when NF is combined with powder catalysts. Hence, nickel foam is an appropriate choice to support CuO-Fe_2O_3, avoiding the loss of catalysts and alleviating its environmental impact.

Herein, we utilized an in situ chemical modification strategy to anchor CuO-Fe_2O_3 catalysts on a supporter without any binders. The CuO-Fe_2O_3-modified nickel foam (CFO-NF) composites were prepared to activate PMS using a one-step hydrothermal method. The optimal synthesis conditions were determined to achieve an efficient PMS activation performance. Then, the morphology, crystal structure, specific surface area, pore structure, and surface functional groups of the composites were characterized. Subsequently, the effect of reaction conditions on the TCs removal was also evaluated in detail, followed by the evaluation of the stability and reusability of CFO-NF. Finally, trapping experiments and electron paramagnetic resonance spectrometry (EPR) detection were utilized to identify the reactive active species and their evolution. The valence transformation of the metal elements in CFO-NF was detected by X-ray photoelectron spectroscopy (XPS) to uncover the mechanism of a catalytic reaction.

2. Results and Discussion

2.1. The Characterizations of CFO-NF Composites

The morphologies of NF, CFO, and CFO-NF were observed by SEM (Figure 1a–e). Pure NF exhibits a typical 3D porous network structure with smooth surfaces, along with abundant channels (about 150–300 μm in pore size) (Figure 1a). Figure 1b,c shows that nanoscale CuO (~20 nm in diameter) and Fe_2O_3 (~40 nm in diameter) were bonded together tightly. The nano CuO and Fe_2O_3 particles tended to agglomerate into bulk. After loading the CFO on NF (Figure 1d), CFO was evenly distributed on the surface of NF. Moreover, CuO and Fe_2O_3 could be adhered firmly to NF (Figure 1e). The EDS element analysis confirmed the existence of Fe, Cu, Ni, and O in CFO-NF (Figure 1f). In addition, the overlapping of Fe, Cu, Ni, and O in elemental mappings (Figure 1g) proved that CuO and Fe_2O_3 were more dispersed after loading on the NF surface compared with CFO. All these results verified that CFO-NF was successfully synthesized by a one-step hydrothermal method.

The XRD patterns of NF and CFO-NF were utilized to analyze their crystal structure. As shown in Figure 2a, three distinct characteristic peaks at 2θ = 44.5°, 51.8°, and 76.4° which emerged in the XRD patterns of pure NF and CFO-NF corresponded to (111), (200), and (220) crystal planes of metal nickel (JCPDS 87-0712) [18]. However, no obvious characteristic peaks of CuO or Fe_2O_3 were observed in the CFO-NF pattern, which might be due to the relatively low loading content of CFO on NF (about 3 wt%) [19]. When the patterns at 30°–40° were magnified (Figure 2b), three characteristic peaks emerged in the CFO-NF pattern compared with that of NF. The peak at 33.2° was indexed to the (104) plane of Fe_2O_3 (JCPDS 33-0664), while the peaks at 35.5° and 38.7° corresponded to the (002) and (111) planes of CuO (JCPDS 45-0937) [20,21]. Moreover, no impurity peak was observed in the XRD patterns, indicating the high purity of the as-prepared CFO-NF catalyst. The result confirmed that CFO adhered to NF tightly.

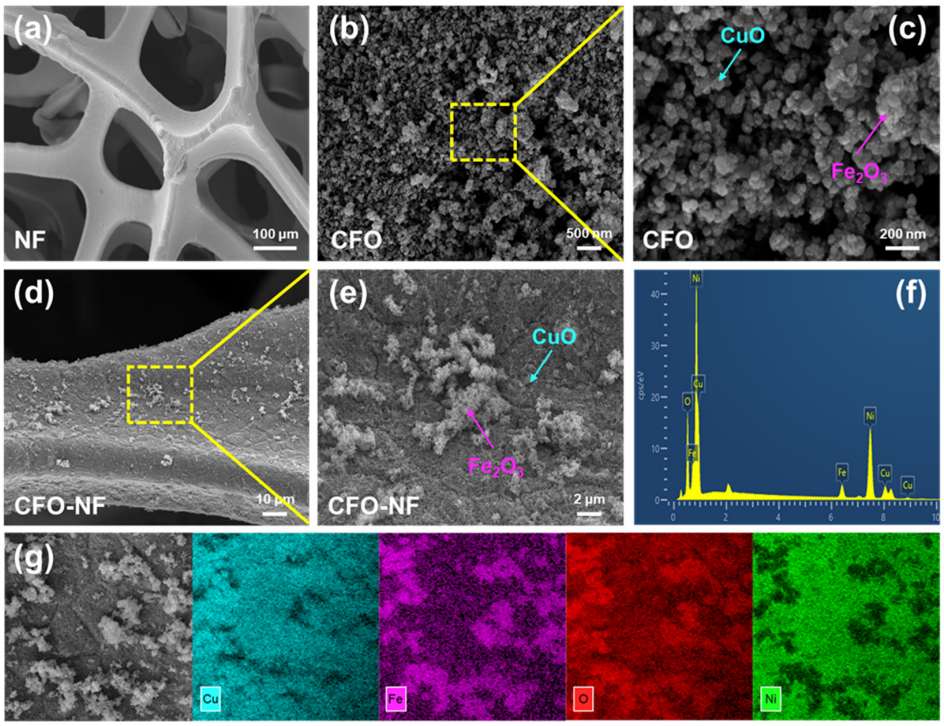

Figure 1. SEM images of (**a**) NF, (**b**,**c**) CFO, and (**d**,**e**) CFO-NF (the yellow box indicates the enlarged portion); (**f**) EDS element analysis of CFO-NF, and (**g**) EDS mappings of CFO-NF.

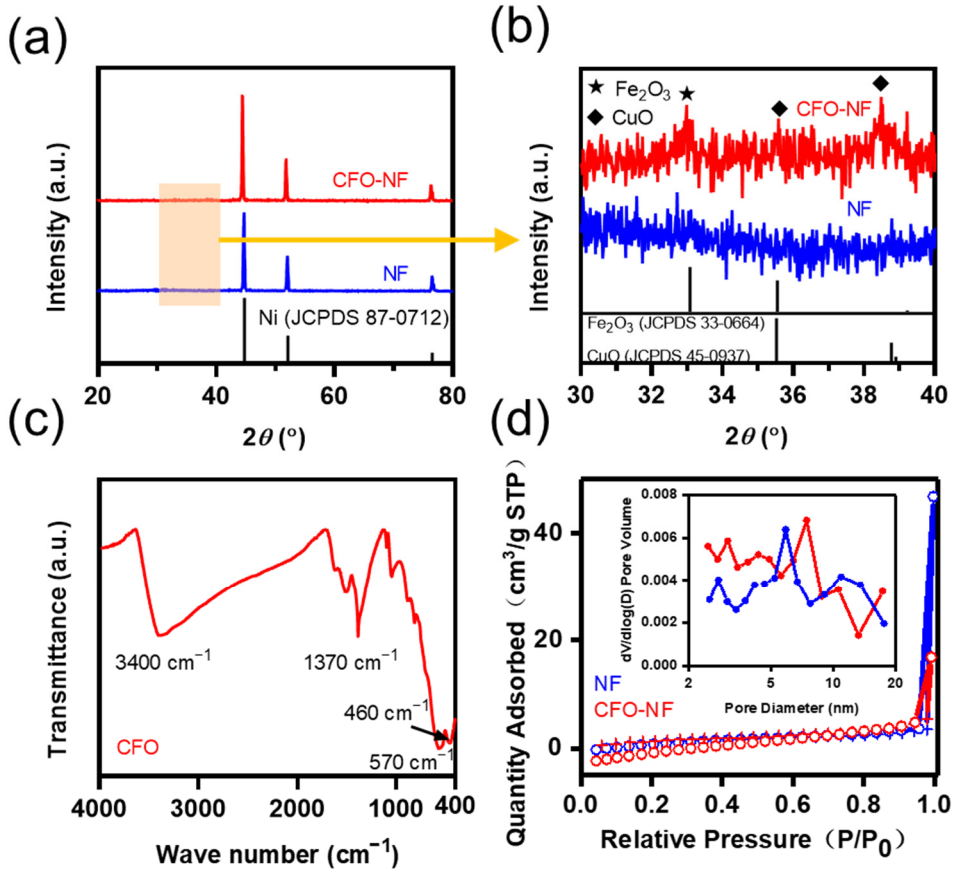

Figure 2. (**a**,**b**) XRD patterns of NF and CFO-NF, (**c**) FTIR spectra of CFO scratched from CFO-NF, (**d**) N_2 adsorption/desorption isotherms of NF and CFO-NF (insert: Barrett-Joyner-Halenda (BJH) analyzes).

A similar phenomenon was also found that no difference was observed in the FTIR spectra of NF and CFO-NF (Figure S1). Additionally, Figure 2c shows the FTIR spectrum of CFO scratched from CFO-NF. The peaks at 460 cm^{-1} and 570 cm^{-1} were attributed to Cu−O vibration in CuO and Fe−O vibration in Fe_2O_3, respectively [22,23]. In addition, the peak at 1370 cm^{-1} was assigned to the O−H bending vibration. The broad peak at about 3400 cm^{-1} was caused by the O−H stretching vibration of the absorbed water on the catalyst [24].

N_2 adsorption–desorption curves were utilized to analyze the textural structure of the as-prepared catalysts. As shown in Figure S2, the adsorption–desorption isotherm of CFO scratched from CFO-NF shows a typical IV curve with a type H3 hysteresis loop, indicating the existence of mesoporous structures in CFO [4]. In addition, the pore sizes in CFO were concentrated at 13 nm and 34 nm, indicating the coexistence of CuO and Fe_2O_3 (insert in Figure S2). Table S1 shows that the average pore size of CFO was 14.91 nm, further proving that CFO was a mesoporous catalyst. In addition, the adsorption–desorption isotherms of NF and CFO-NF were also classified as typical IV curves with a type H3 adsorption hysteresis loop (Figure 2d). The pristine NF possessed smooth surfaces (Figure 1a), resulting in a low N_2 sorption amount and a small specific surface area (3.87 m^2 g^{-1}) [25]. After loading the CFO, a 10% increase in the specific surface area was obtained, illustrating the adherent CFO on the surface of NF and confirming the combination of CFO and NF.

2.2. Performance of CFO-NF for TC Degradation

2.2.1. Effects of Synthesis Conditions on TC Degradation

Before the test for the catalytic performance of the catalysts, the TC detection accuracy by a UV/Vis spectrophotometer was determined, meeting the experimental requirements well (Figure S3). The adsorption performance of CFO-NF towards TC was evaluated. According to Figure S4, adsorption equilibrium was achieved within 30 min. Hence, the time for adsorption equilibrium was determined to be 30 min in the following experiments. The degradation performance of the different systems was estimated in Figure 3a. About 70.1% TC could be removed within 60 min when only PMS was added. The addition of NF had a slight improvement in the TC degradation (~73.9%), which indicated that pristine NF was not an effective catalyst for activating PMS. After NF was modified with CFO, the CFO-NF composite could achieve a 97.9% TC degradation efficiency within 60 min, which was 40% and 32% higher than that of PMS and NF/PMS systems, respectively. These results confirmed that the modification of NF with CFO was successful, and CFO-NF was a strong catalyst for the PMSs activation.

Then, the synthetic conditions for a series of CFO-NF composites were optimized (Figure 3b–d). Figure 3b shows the effect of the different mass ratios of CFO to NF (CFO:NF) on the TC degradation efficiency. The degradation efficiency increased from 79.1% to 94.0% with CFO:NF from 7:1 to 11:1, meaning that more loading of CFO could enhance the catalytic performance due to an increased active ingredient. However, further increasing the mass ratio of CFO:NF to 14:1 and 21:1 would harm the catalytic performance (90.4% and 66.7%, respectively), which was caused by the saturation of the actual loading ratio and the existence of synergistic effect between CFO and NF [26,27]. In addition, the synthetic time and temperature also affected the property of the catalyst. Figure 3c exhibits the influence of synthetic time on the degradation efficiency. The TC degradation efficiency reached the maximum (94%) when the hydrothermal time was 1 h. Appropriate hydrothermal time could promote the formation of the catalyst. However, exceeding the energy input harmed the crystal structure, damaging the removal efficiency (85.7% for 2.5 h). As shown in Figure 3d, a higher temperature (160 °C) was beneficial to improve the catalytic performance (97.9%). In contrast, an excessive temperature would decrease the catalytic performance (94.2% at 170 °C to 88.5% at 190 °C) because a superfluous energy input would cause the agglomeration of the catalyst [28].

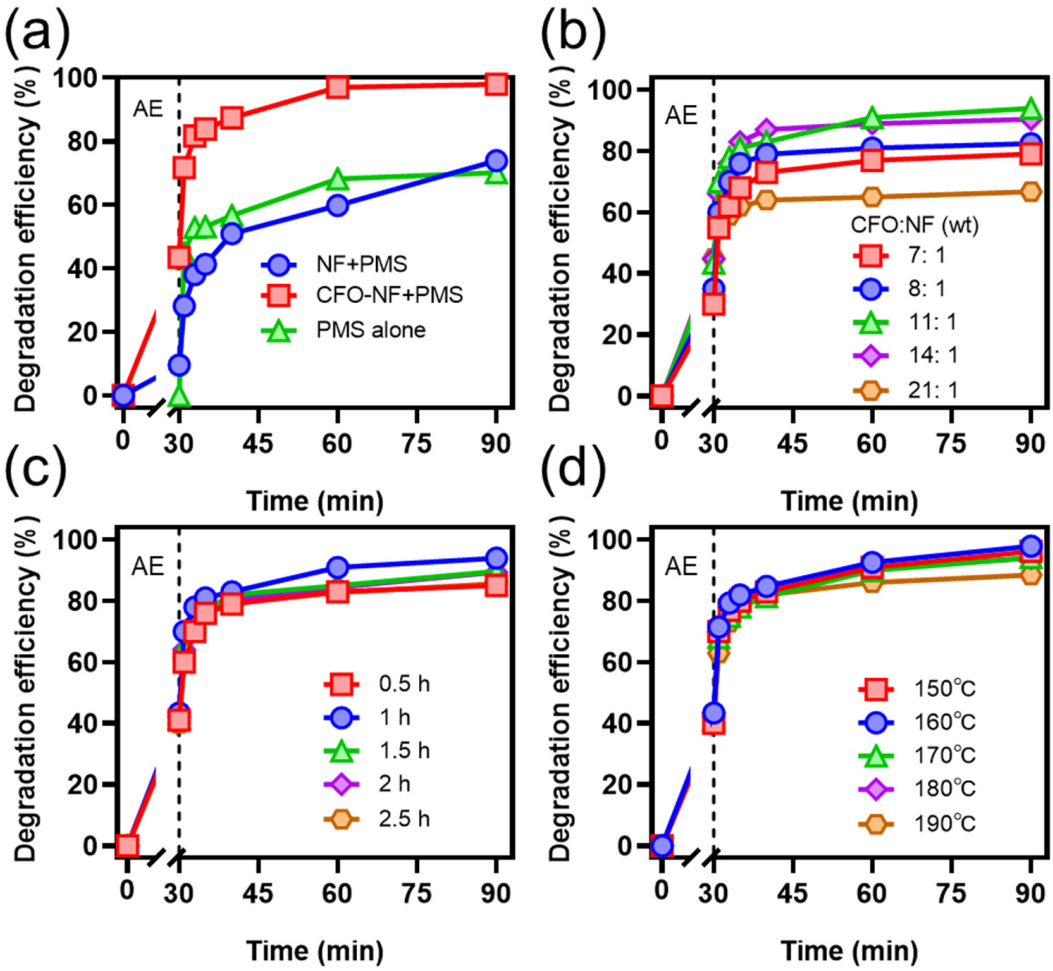

Figure 3. Effect of (**a**) different systems (PMS: 0.4 mM, TC: 10 mg L^{-1}, catalysts: 4 pieces, 25 °C), (**b**) the mass ratio of CFO to NF, (**c**) hydrothermal time (180 °C), and (**d**) hydrothermal temperature on TC degradation efficiency ((**b**–**d**): PMS: 0.7 mM, TC: 10 mg L^{-1}, catalysts: 4 pieces, 25 °C) (Note: AE represents adsorption equilibrium).

2.2.2. Effects of Reaction Conditions on TC Degradation

The influence of the PMS concentration and CFO-NF dosage on the TC degradation efficiency was displayed in Figure 4. When the PMS concentration increased from 0.20 mM to 0.40 mM, the degradation efficiency increased to 97.9% within 60 min. However, when further increasing the PMS concentration to 1.00 mM, the degradation performance was not strengthened. On the one hand, excess PMS would quench the active species, inhibiting the degradation performance [29]. On the other hand, a fixed amount of CFO-NF possessed limited active sites, which led to the ineffective activation of the PMS [30]. Hence, the optimal PMS concentration was 0.40 mM. Figure 4b shows the effect of the catalyst dosage on the degradation performance. The degradation efficiency increased with the dosage of CFO-NF, whereas excess catalyst did not positively affect the degradation efficiency. This might be ascribed to the quenching effect of extra catalyst [31]. Four pieces of catalyst was the optimal dosage based on the cost-effective principle.

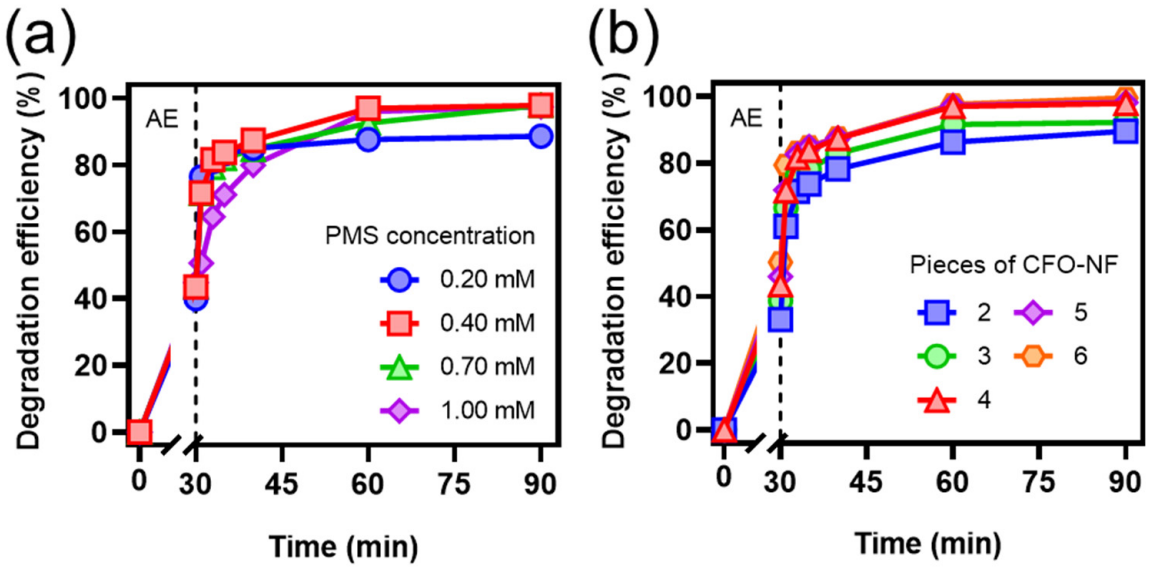

Figure 4. Effect of (**a**) PMS concentration (TC: 10 mg L^{-1}, catalysts: 4 pieces, 25 °C), and (**b**) the amount of CFO-NF (TC: 10 mg L^{-1}, PMS: 0.4 mM, 25 °C) on TC degradation efficiency (Note: AE represents adsorption equilibrium).

2.3. Stability of CFO-NF Composites

The stability and reusability of CFO-NF are significant properties for its practical applications in wastewater treatment. Hence, the recycle experiments were conducted under identical conditions (Figure 5a). The CFO-NF catalyst could be reused after facilely removing from the reaction solution and cleaning, which was of benefit to the post-separation of the catalyst. The degradation efficiency could maintain >85% even after five consecutive degradation cycles, indicating the excellent reusability and stability of CFO-NF. The slight decrease in the degradation efficiency would be caused by the shelter of active sites by a generated degradation intermediate and the unavoidable loss of reactive species [32].

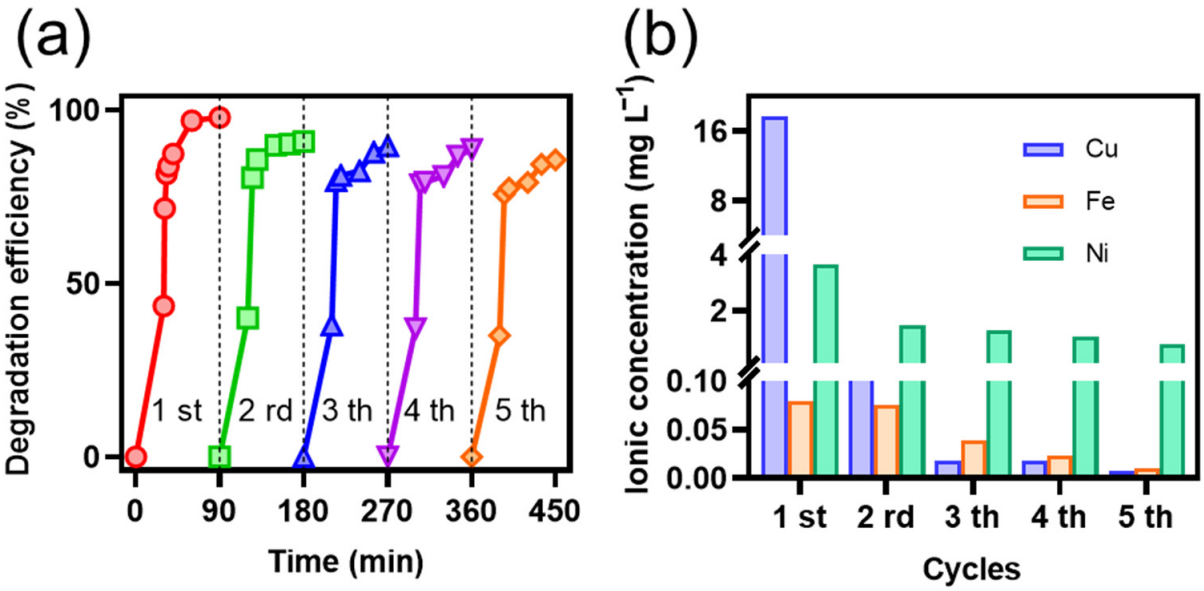

Figure 5. (**a**) The TC degradation efficiency over five cycles in CFO-NF/PMS system, and (**b**) ion dissolution over five cycles in CFO-NF/PMS system (PMS: 0.4 mM, TC: 10 mg L^{-1}, catalysts: 4 pieces, 25 °C).

The leaching of the metal ions (Cu, Fe, and Ni) was monitored during the cycle experiments, as displayed in Figure 5b. The concentration of leached Cu ion declined from 17.71 mg L^{-1} to 7.07 μg L^{-1} after five cycles. In addition, the leaching Cu ion concentration decreased by 99.43% after two cycles. In addition, the Fe and Ni ion concentrations decreased from 0.08 mg L^{-1} and 3.67 mg L^{-1} to 9.51 μg L^{-1} and 0.80 mg L^{-1}, respectively. Based on the slight decrease in the degradation efficiency during the cycle experiments, the reduction in the metal ion dissolution with cycle numbers resulted from the loss of unstable and invalid metal ions, which also accounted for the striking difference in the concentration of metal ions between the first cycle and the rest of the cycles [33].

2.4. Mechanism for PMS Activation and TC Degradation

2.4.1. Identification of Actives Species

The active species generated in the catalytic process was determined by trapping experiments, as shown in (Figure 6a). TBA quenched •OH with a rate constant of 6.0×10^8 M^{-1} s^{-1} [34]. MeOH was used to trap both •OH and $SO_4^{\bullet-}$ with the rate constants of 1.6–7.7 $\times$ 10^7 M^{-1} s^{-1} and 1.2–2.8 $\times$ 10^9 M^{-1} s^{-1}, respectively [35]. Hence, the difference in the degradation efficiency between the TBA and MeOH could be utilized to distinguish the contribution of •OH and $SO_4^{\bullet-}$. The degradation efficiency decreased from 89.5% to 85.9% as the concentration of TBA increased from 10:1 to 100:1. The adverse impact of TBA on the degradation efficiency was stable and limited, meaning that •OH could be completed quenched and the contribution of •OH to the TC degradation was restricted. When MeOH with different concentrations was added to the system, the degradation efficiency declined to ~58%, with the MeOH: PMS increasing from 10:1 to 100:1. Hence, the contribution of $SO_4^{\bullet-}$ could be determined to ~27.9%. Moreover, a similar phenomenon to TBA indicated that $SO_4^{\bullet-}$ was not the main active species in the system. In addition, L-histidine could efficiently scavenge the $^1O_2$ produced with a rate constant of 3.2×10^7 M^{-1} s^{-1} [36]. When L-histidine (L-histidine: PMS = 1:1) was added to the system, a robust inhibitory effect on the TC degradation was observed (40%). When increasing L-histidine: PMS from 1:1 to 3:1, the degradation process was almost completely suppressed (~5.4%). This result confirmed that $^1O_2$ was the main active species and played a crucial role in the catalytic degradation. In addition, the inhibition of TEMPO on the degradation efficiency increased from 26.1% to 36.5% when the concentration of TEMPO increased [37], meaning that $O_2^{\bullet-}$ also played a role in the catalytic process.

EPR spectroscopy was also used to detect the active species during the process (Figure 6b–d). As displayed in Figure 5b, the characteristic signal of DMPO−•OH (a_H = 15.0 G and a_N = 14.9 G, peak intensities of 1:2:2:1) was identified [38], displaying the existence of •OH. In addition, the intensity of the DMPO−•OH characteristic signal did not increase as the reaction continued, consistent with the result of the trapping experiments. However, the typical signal of DMPO−$SO_4^{\bullet-}$ was not observed in Figure 6b, indicating the relatively low concentration of $SO_4^{\bullet-}$. Interestingly, a carbon-centric radical DMPOD generated by DMPO oxidation was found [39], showing the strong oxidation capacity of the system. In addition, the TEMP-$^1O_2$ signal with triplet peaks (1:1:1) was also found in the CFO-NF/PMS system (Figure 6c) and the signal intensity increased with the reaction process. This proved the production of $^1O_2$ and its concentration increased with the reaction. The signal of DMPO−$O_2^{\bullet-}$ was also detected in the system (Figure 6d), and its signal increased with the reaction. Generated $O_2^{\bullet-}$ could further be transformed into $^1O_2$ as a precursor [40]. Hence, it was also a critical piece of evidence to prove the vital role of $^1O_2$ in TC degradation. In general, the TC degradation process was mainly a non-radical pathway dominated by $^1O_2$.

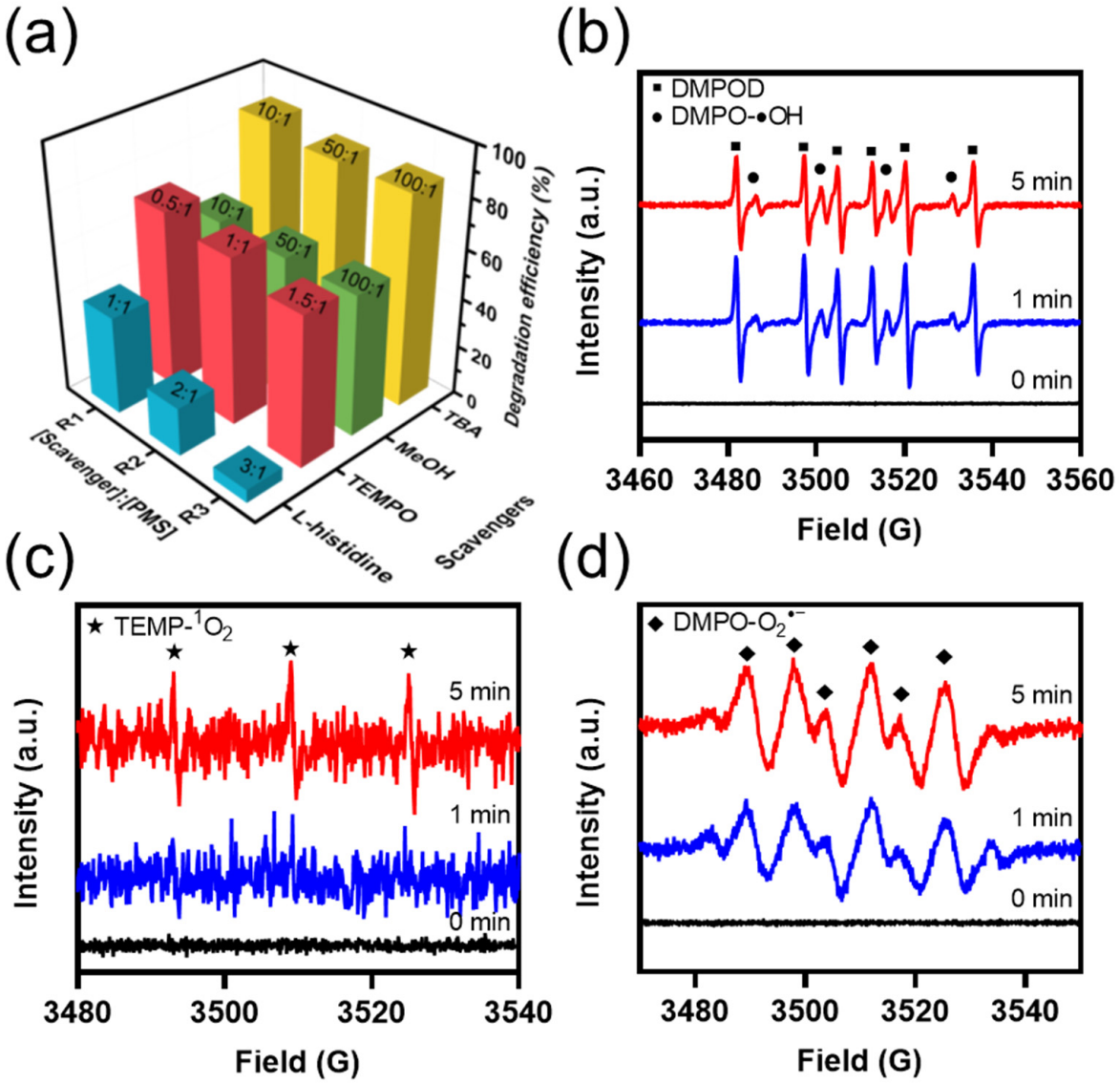

Figure 6. (**a**) Trapping experiments with different scavengers (the molar ratio of scavengers to PMS); EPR spectra for (**b**) •OH and $SO_4^{\bullet-}$, (**c**) $^1O_2$ and (**d**) $O_2^{\bullet-}$.

2.4.2. Catalytic Mechanisms of the CFO-NF/PMS System

The XPS spectra of fresh and used catalysts were utilized to explore further the catalytic mechanism in the CFO-NF/PMS system (Figure 7 and Table S2). As shown in Figure 7a, Cu, Fe, Ni, and O were all detected in the XPS survey spectra of fresh and used catalysts. All XPS spectra were revised based on the peak of C−C at 284.8 eV, as shown in the C 1s spectrum (Figure 7b). Figure 7c shows the Cu 2p spectrum. The peaks at 934.3 eV and 953.7 eV in the fresh catalyst corresponded to Cu $2p_{3/2}$ and $2p_{1/2}$, while the peaks at 942.5 eV and 962.3 eV were the satellite peaks of Cu(II). After the catalytic reaction, the new peaks at 932.1 eV and 952.1 eV emerged in the spectrum, ascribed to the characteristic signal of Cu(I) (78.6%). The presence of Cu(I) confirmed the existence of the cycle of Cu(II)/Cu(I). Cu(II)/Cu(I) could react with HSO_5^- to produce various radicals ($SO_5^{\bullet-}$, $SO_4^{\bullet-}$, •OH) (Equations (1)–(3)) [41]. As displayed in Figure 7d, the peaks at 710.9 eV, 723.9 eV, 718.5 eV, and 733.5 eV in the Fe 2p spectrum of the fresh catalyst were assigned to Fe $2p_{3/2}$, Fe $2p_{1/2}$, and the satellite peaks of Fe(III), confirming the existence of Fe_2O_3 in CFO-NF [42]. After the reaction, the new peaks emerged at 710.8 eV and 723.6 eV belonged to Fe(II) $2p_{3/2}$ and Fe(II) $2p_{1/2}$, which proved the reduction in Fe(III) to Fe(II) (36.1%) (Equation (4)). The generated Fe(II) could also react with HSO_5^- to form $SO_4^{\bullet-}$

(Equation (5)). However, the reaction between Fe(III) and HSO_5^- was thermodynamically infeasible (E^0(Fe(III)/Fe(II)) = 0.77 V < E^0($SO_5^{\bullet-}$/HSO_5^-) = 1.10 V) [43]. In Figure 7e, three forms of Ni (Ni(II), Ni(III), and Ni0) were confirmed both in the spectra of fresh and used catalysts [44,45]. Specifically, the peaks at 853.8 eV and 871.6 eV were attributed to Ni(II), the peaks at 855.8 eV and 874.0 eV were responsible for Ni(III), while the peaks at 852.7 eV and 869.9 eV were ascribed to Ni^0. These results confirmed the existence of nickel foam and the chemical bonding between CFO and NF. Moreover, the content variations in Ni(II) (−31.1%) and Ni(III) (+25.4%) proved that Ni could also participate in the redox reaction for the TC degradation (Equations (6)–(8)) and the synergistic effect between CFO and NF could further promote the catalytic performance. In the O 1s XPS spectra (Figure 7f), the peaks at 529.7 eV and 531.8 eV were ascribed to the lattice oxygen (O_{lat}) and oxygen vacancy (O_V), respectively. O_V could react with HSO_5^-, which was responsible for the generation of $O_2^{\bullet-}$ (Equation (9)). $O_2^{\bullet-}$ could further transform to $^1O_2$ (Equation (10)) [46]. The relative O_{lat} content decreased after the reaction (1.2%), indicating that O_{lat} could take part in the reaction to generate further $^1O_2$ (Equations (11) and (12)) [47]. Moreover, $^1O_2$ could also be produced through the self-reaction of $SO_5^{\bullet-}$ (Equation (13)) [48]. In addition, a new peak at 532.5 eV emerged in the spectrum of the used catalyst and was assigned to the oxygen in adsorbed H_2O.

$$Cu(II) + HSO_5^- \rightarrow Cu(I) + SO_5^{\bullet-} + H^+ \quad (1)$$

$$Cu(I) + HSO_5^- \rightarrow Cu(II) + SO_4^{\bullet-} + OH^- \quad (2)$$

$$Cu(I) + HSO_5^- \rightarrow Cu(II) + SO_4^{2-} + \bullet OH \quad (3)$$

$$Cu(I) + Fe(III) \rightarrow Cu(II) + Fe(II) \quad (4)$$

$$Fe(II) + HSO_5^- \rightarrow Fe(III) + SO_4^{\bullet-} + OH^- \quad (5)$$

$$Cu(I) + Ni(III) \rightarrow Cu(II) + Ni(II) \quad (6)$$

$$Fe(II) + Ni(III) \rightarrow Fe(III) + Ni(II) \quad (7)$$

$$Ni(II) + HSO_5^- \rightarrow Ni(III) + SO_4^{\bullet-} + OH^- \quad (8)$$

$$HSO_5^- + 2O_V \rightarrow O_2^{\bullet-} + 2HSO_4^- \quad (9)$$

$$2O_2^{\bullet-} + 2H_2O \rightarrow {}^1O_2 + 2OH^- + H_2O_2 \quad (10)$$

$$O_{lat} \rightarrow O^* \quad (11)$$

$$O^* + HSO_5^- \rightarrow {}^1O_2 + HSO_4^- \quad (12)$$

$$SO_5^{\bullet-} + SO_5^{\bullet-} \rightarrow 2SO_4^{2-} + {}^1O_2 \quad (13)$$

Based on the above discussion, the reasonable catalytic mechanism of the PMSs activation for the TC degradation in the CFO-NF/PMS system was proposed. Nickel foam not only functioned as a supporter but also took part in the redox reaction for a 98% TC degradation. The valence conversion among Fe(II)/Fe(III), Cu(I)/Cu(II), and Ni(II)/Ni(III) promoted the reaction with PMS, further producing lots of active species, in which the non-radical pathway represented by $^1O_2$ played a dominate role. $O_2^{\bullet-}$, O_{lat}, and $SO_5^{\bullet-}$ were responsible for the generation of $^1O_2$, accounting for the vital role of $^1O_2$ in the degradation process.

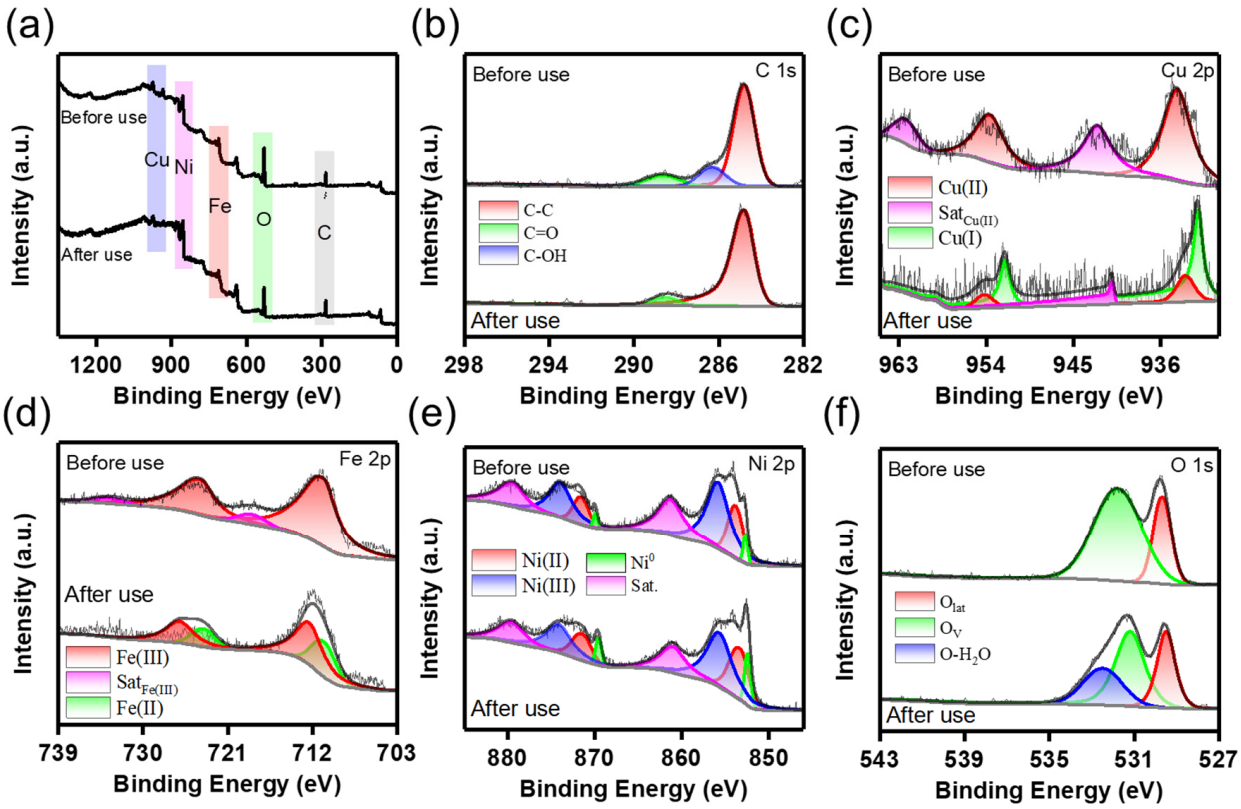

Figure 7. XPS spectra of fresh and used CFO-NF: (**a**) survey spectra, (**b**) C 1s, (**c**) Cu 2p, (**d**) Fe 2p, (**e**) Ni 2p, and (**f**) O 1s.

3. Materials and Methods

3.1. Materials

In this study, NF was purchased from JiaShiDe Foam Metal Co., Ltd. (Suzhou, China). Acetone, hydrochloric acid (HCl), anhydrous ethanol, urea, iron nitrate nonahydrate ($Fe(NO_3)_3{\cdot}9H_2O$), copper nitrate trihydrate ($Cu(NO_3)_3{\cdot}3H_2O$), methanol (MeOH), tert-butanol (TBA), and L-histidine were purchased from Tianjin Beilian Fine Chemicals Development Co., Ltd. Tetracycline hydrochloride (TC) and PMS ($KHSO_5{\cdot}0.5KHSO_4{\cdot}K_2SO_4$) were obtained from Macklin, China. 2,2,6,6-tetramethylpiperidine 1-oxyl (TEMPO), 4-amino-2,2,6,6-tetramethylpiperidine (TEMP), and 5,5-dimethyl-1-pyrroline N-oxide (DMPO) were acquired from Aladdin, China. All of the reagents above were of an analytical grade or higher and were used without a further purification. Deionized (DI) water was used throughout the experiments.

3.2. Fabrication of CFO-NF Composites

Pretreatment for NF. The pretreatment method of NF refers to our previous study [27]. Specifically, NF was pretreated to remove the impurities on the surface. First, pre-cut (10 mm × 10 mm × 1 mm) nickel foam pieces were immersed in acetone with ultrasonic for 30 min to clean up the extra organic compounds, followed by rinsing with DI water several times. Then, the NF pieces were transformed into a 10 mM HCl solution and were soaked for 30 min to eliminate the extra metal ions. After that, the NF pieces were washed with DI water until the pH was neutral. Finally, the NF pieces were dried in a vacuum oven (BZF-50) at 60 °C for further use.

Synthesis of CFO-NF. A series of CFO-NF composites were synthesized using a hydrothermal method. Typically, 0.242 g of $Cu(NO_3)_3{\cdot}3H_2O$, 0.808 g of $Fe(NO_3)_3{\cdot}9H_2O$, and 0.300 g of urea were added to 20 mL of DI water under continuous stirring for 30 min. Then, four pieces of NF were added to the above solution by stirring magnetically for

30 min. The precursor solution was transferred to a Teflon reaction tank in an electric thermostatic drying oven (WHL-25AB, Tianjin Taiste Instrument Co., Ltd., Tianjin, China) and then reacted at 160 for 1 h. After cooling naturally to room temperature, the modified NF was washed with DI water and anhydrous ethanol several times and was then vacuum dried at 60 °C overnight. The CFO-NF catalysts were finally obtained. Pure CuO-Fe_2O_3 (CFO) was synthesized using the same method without adding NF.

3.3. Characterizations

The crystal structures of CFO and CFO-NF were characterized with an X-ray diffractometer (XRD, D/max-rB, Rigaku, Tokyo, Japan) with Cu Kα1 (λ = 0.154 nm) irradiation (a scanning range of 5−90° and a scanning speed of 0.2°/0.4 s). A scanning electron microscope (SEM, Sigma500, Zeiss, Oberkochen, Germany) equipped with energy dispersive spectral analysis (EDS) was used to observe the morphologies and microstructures of the composites. The specific surface areas of the catalysts were analyzed by a surface area and porosity analyzer (ASAP2460, Micromeritics, Norcross, GA, USA). The elemental compositions and chemical states of the catalysts were analyzed by X-ray photoelectron spectroscopy (XPS, Thermo Scientific ESCALAB Xi+, Thermo Fisher, Waltham, MA, USA). The surface functional groups of the catalysts were measured using Fourier transform infrared spectroscopy (FTIR, Thermo Scientific Nicolet iS20, Thermo Fisher, USA) with KBr powder as the reference transmittance in a wavenumber range of 400–4000 nm^{-1}.

3.4. Experimental Procedures

The optimization of the synthesis conditions and performance of the catalysts for the PMSs activation was evaluated through the TC degradation efficiency. The catalytic experiments were conducted in a 100 mL glass beaker. Typically, a certain amount of the as-prepared catalyst was added to 50 mL of TC solution (10 mg L^{-1}). After stirring magnetically for 30 min to achieve an adsorption equilibrium, the degradation experiments were initiated when adding PMS into the suspension. During the reaction, 1 mL of reactant suspension was withdrawn at specific time intervals, filtered through 0.22 μm filters into autosampler vials, and transferred in an ice water bath immediately to stop the reaction. Finally, the samples were stored at 4 °C for a further analysis.

3.5. Analytical Methods

The TC concentration was measured by a UV/Vis spectrophotometer. The detection wavelength was 357 nm. The leaching metal ion concentrations were monitored by an inductively coupled plasma atomic emission spectrometer (ICP-AES, Optima 5300DV, PerkinElmer, Waltham, MA, USA).

The main reactive oxygen species (ROS) were identified through trapping experiments. MeOH was chosen to quench both •OH and $SO_4^{\bullet-}$, and TBA was selected as the scavenging agent for •OH. TEMPO was selected to quench $O_2^{\bullet-}$, while L-histidine trapped $^1O_2$. The experimental procedures were the same as the degradation experiments except for adding scavengers. In addition, electron paramagnetic resonance spectrometry (EPR, A300E, Bruker, Heidelberg, Germany) was employed to detect ROS in the system. DMPO was used to detect the spin adducts of •OH, $SO_4^{\bullet-}$, and $O_2^{\bullet-}$. TEMP was used for the detection of $^1O_2$.

4. Conclusions

In this study, CuO-Fe_2O_3-modified Ni foam was fabricated using a facile hydrothermal method for an efficient PMS activation and TC degradation. The optimal CFO-NF was synthesized with CFO:NF =11:1 at 180 °C for 1 h. The CFO-NF/PMS system could achieve a 97.9% TC removal efficiency in 60 min with four pieces of CFO-NF and 0.4 mmol L^{-1} of PMS. The removal efficiency was maintained at >85% after five cycles, accounting for the excellent stability of the CFO-NF composites. The valence conversion among Fe(II)/Fe(III), Cu(I)/Cu(II), and Ni(II)/Ni(III) promoted the PMSs activation, further resulting in the

production of active species (•OH, $SO_4^{\bullet-}$, $O_2^{\bullet-}$, and $^1O_2$), in which $^1O_2$ played a dominate role. Besides being a supporter, NF could also synergistically activate PMS. This study provides a novel avenue for fabricating CuO-Fe_2O_3-modified Ni foam with a superior PMS activation performance, a high stability, and a recoverability for eliminating the refractory organic pollutants.

Supplementary Materials: The following supporting information can be downloaded at: https://www.mdpi.com/article/10.3390/catal13020329/s1, Figure S1: FTIR spectra of NF and CFO-NF; Figure S2: N_2 adsorption/desorption isotherms of CFO scratched from CFO-NF (insert: Barrett-Joyner-Halenda (BJH) analyzes); Figure S3: The standard curve of TC; Figure S4: The adsorption performance of CFO-NF towards TC; Table S1: Specific surface areas and pore characteristics of different catalysts; Table S2: The content of various elements in fresh and used catalysts.

Author Contributions: X.R.: methodology, investigation, and data curation; P.X.: writing—original draft preparation and writing—review and editing; K.T.: investigation; M.C.: investigation; F.S.: investigation; G.Z.: conceptualization, writing—review and editing, supervision, and funding acquisition. All authors have read and agreed to the published version of the manuscript.

Funding: The work was supported by Natural Science Foundation of Shandong Province, China (ZR2022ME128), Open Project of State Key Laboratory of Urban Water Resource and Environment, Harbin Institute of Technology (ES202206), Talents of High-Level Scientific Research Foundation of Qingdao Agricultural University (6651120004), and ShanDong Students' Platform for innovation and entrepreneurship training program (S202110435085) for their financial support.

Data Availability Statement: The data presented in this study are available on request from the corresponding author. The data are not publicly available due to privacy.

Conflicts of Interest: The authors declare no conflict of interest.

References

1. Xie, J.L.; Chen, L.; Luo, X.; Huang, L.; Li, S.Y.; Gong, X.B. Degradation of tetracycline hydrochloride through efficient peroxymonosulfate activation by B, N co-doped porous carbon materials derived from metal-organic frameworks: Nonradical pathway mechanism. *Sep. Purif. Technol.* **2022**, *281*, 119887. [CrossRef]
2. Peng, X.M.; Wu, J.Q.; Zhao, Z.L.; Wang, X.; Dai, H.L.; Xu, L.; Xu, G.P.; Jian, Y.; Hu, F.P. Activation of peroxymonosulfate by single-atom Fe-g-C_3N_4 catalysts for high efficiency degradation of tetracycline via nonradical pathways: Role of high-valent iron-oxo species and Fe-N_X sites. *Chem. Eng. J.* **2022**, *427*, 130803. [CrossRef]
3. Xu, L.Y.; Zhang, H.; Xiong, P.; Zhu, Q.Q.; Liao, C.Y.; Jiang, G.B. Occurrence, fate, and risk assessment of typical tetracycline antibiotics in the aquatic environment: A review. *Sci. Total Environ.* **2021**, *753*, 141975. [CrossRef]
4. Xu, P.; Wang, P.; Li, X.; Wei, R.; Wang, X.; Yang, C.; Shen, T.; Zheng, T.; Zhang, G. Efficient peroxymonosulfate activation by CuO-Fe_2O_3/MXene composite for atrazine degradation: Performance, coexisting matter influence and mechanism. *Chem. Eng. J.* **2022**, *440*, 135863. [CrossRef]
5. Qu, J.H.; Tian, X.; Zhang, X.B.; Yao, J.Y.; Xue, J.Q.; Li, K.G.; Zhang, B.; Wang, L.; Zhang, Y. Free radicals-triggered reductive and oxidative degradation of highly chlorinated compounds via regulation of heat-activated persulfate by low-molecular-weight organic acids. *Appl. Catal. B-Environ.* **2022**, *310*, 121359. [CrossRef]
6. Milh, H.; Cabooter, D.; Dewil, R. Role of process parameters in the degradation of sulfamethoxazole by heat-activated peroxymonosulfate oxidation: Radical identification and elucidation of the degradation mechanism. *Chem. Eng. J.* **2021**, *422*, 130457. [CrossRef]
7. Qu, J.H.; Xu, Y.; Zhang, X.B.; Sun, M.Z.; Tao, Y.; Zhang, X.M.; Zhang, G.S.; Ge, C.J.; Zhang, Y. Ball milling-assisted preparation of N-doped biochar loaded with ferrous sulfide as persulfate activator for phenol degradation: Multiple active sites-triggered radical/non-radical mechanism. *Appl. Catal. B-Environ.* **2022**, *316*, 121639. [CrossRef]
8. Guan, Y.H.; Ma, J.; Li, X.C.; Fang, J.Y.; Chen, L.W. Influence of pH on the Formation of Sulfate and Hydroxyl Radicals in the UV/Peroxymonosulfate System. *Environ. Sci. Technol.* **2011**, *45*, 9308–9314. [CrossRef]
9. Chen, Y.X.; Lan, S.Y.; Zhu, M.S. Construction of piezoelectric $BaTiO_3$/MoS_2 heterojunction for boosting piezo-activation of peroxymonosulfate. *Chin. Chem. Lett.* **2021**, *32*, 2052–2056. [CrossRef]
10. Gao, Q.; Wang, G.S.; Chen, Y.R.; Han, B.; Xia, K.S.; Zhou, C.G. Utilizing cobalt-doped materials as heterogeneous catalysts to activate peroxymonosulfate for organic pollutant degradation: A critical review. *Environ. Sci.-Wat. Res. Technol.* **2021**, *7*, 1197–1211. [CrossRef]
11. Tian, K.; Hu, L.M.; Li, L.T.; Zheng, Q.Z.; Xin, Y.J.; Zhang, G.S. Recent advances in persulfate-based advanced oxidation processes for organic wastewater treatment. *Chin. Chem. Lett.* **2022**, *33*, 4461–4477. [CrossRef]

12. Ding, P.J.; Niu, J.R.; Chang, F.Q.; He, Z.; Wagberg, T.; Li, Z.X.; Hu, G.Z. $NiCo_2O_4$ hollow microsphere-mediated ultrafast peroxymonosulfate activation for dye degradation. *Chin. Chem. Lett.* **2021**, *32*, 2495–2498. [CrossRef]
13. Hu, L.M.; Zhang, G.S.; Liu, M.; Wang, Q.; Wang, P. Enhanced degradation of Bisphenol A (BPA) by peroxymonosulfate with Co_3O_4-Bi_2O_3 catalyst activation: Effects of pH, inorganic anions, and water matrix. *Chem. Eng. J.* **2018**, *338*, 300–310. [CrossRef]
14. Duan, L.X.; Zhou, X.J.; Liu, S.T.; Shi, P.H.; Yao, W.F. 3D-hierarchically structured Co_3O_4/graphene hydrogel for catalytic oxidation of Orange II solutions by activation of peroxymonosulfate. *J. Taiwan Inst. Chem. Eng.* **2017**, *76*, 101–108. [CrossRef]
15. Yang, C.Y.; Wang, P.; Li, J.N.; Wang, Q.; Xu, P.; You, S.J.; Zheng, Q.Z.; Zhang, G.S. Photocatalytic PVDF ultrafiltration membrane blended with visible-light responsive Fe(III)-TiO_2 catalyst: Degradation kinetics, catalytic performance and reusability. *Chem. Eng. J.* **2021**, *417*, 129340. [CrossRef]
16. Chen, X.T.; Zhang, T.; Kan, M.; Song, D.G.; Jia, J.P.; Zhao, Y.X.; Qian, X.F. Binderless and Oxygen Vacancies Rich FeNi/Graphitized Mesoporous Carbon/Ni Foam for Electrocatalytic Reduction of Nitrate. *Environ. Sci. Technol.* **2020**, *54*, 13344–13353. [CrossRef]
17. Yuan, R.X.; Hu, L.; Yu, P.; Wang, H.Y.; Wang, Z.H.; Fang, J.Y. Nanostructured Co_3O_4 grown on nickel foam: An efficient and readily recyclable 3D catalyst for heterogeneous peroxymonosulfate activation. *Chemosphere* **2018**, *198*, 204–215. [CrossRef]
18. Jonoush, Z.A.; Rezaee, A.; Ghaffarinejad, A. Electrocatalytic nitrate reduction using Fe^0/Fe_3O_4 nanoparticles immobilized on nickel foam: Selectivity and energy consumption studies. *J. Clean Prod.* **2020**, *242*, 118569. [CrossRef]
19. Ye, Z.H.; Lin, L.Y.; Yu, C.F. Nickel precursor-free synthesis of nickel cobalt sulfide on Ni foam: Effects of the pH value on the morphology and the energy-storage ability. *J. Energy Storage* **2016**, *8*, 60–68. [CrossRef]
20. Li, W.; Li, Y.X.; Zhang, D.Y.; Lan, Y.Q.; Guo, J. CuO-Co_3O_4@CeO_2 as a heterogeneous catalyst for efficient degradation of 2,4-dichlorophenoxyacetic acid by peroxymonosulfate. *J. Hazard. Mater.* **2020**, *381*, 121209. [CrossRef]
21. Ding, M.M.; Chen, W.; Xu, H.; Shen, Z.; Lin, T.; Hu, K.; Lu, C.H.; Xie, Z.L. Novel α-Fe_2O_3/MXene nanocomposite as heterogeneous activator of peroxymonosulfate for the degradation of salicylic acid. *J. Hazard. Mater.* **2020**, *382*, 121064. [CrossRef] [PubMed]
22. Bousalah, D.; Zazoua, H.; Boudjemaa, A.; Benmounah, A.; Messaoud-Boureghda, M.Z.; Bachari, K. Enhanced reactivity of the CuO-Fe_2O_3 intimate heterojunction for the oxidation of quinoline yellow dye (E104). *Environ. Sci. Pollut. Res.* **2022**, *29*, 69988–69999. [CrossRef] [PubMed]
23. Lyu, J.C.; Ge, M.; Hu, Z.; Guo, C.S. One-pot synthesis of magnetic CuO/Fe_2O_3/$CuFe_2O_4$ nanocomposite to activate persulfate for levofloxacin removal: Investigation of efficiency, mechanism and degradation route. *Chem. Eng. J.* **2020**, *389*, 124456. [CrossRef]
24. Xu, P.; Wang, P.; Wang, Q.; Wei, R.; Li, Y.; Xin, Y.; Zheng, T.; Hu, L.; Wang, X.; Zhang, G. Facile synthesis of Ag_2O/ZnO/rGO heterojunction with enhanced photocatalytic activity under simulated solar light: Kinetics and mechanism. *J. Hazard. Mater.* **2021**, *403*, 124011. [CrossRef] [PubMed]
25. Chen, H.H.; Park, Y.K.; Kwon, E.; Tsang, Y.F.; Thanh, B.X.; Khiem, T.C.; You, S.M.; Hu, C.C.; Lin, K.Y.A. Nanoneedle-Assembled Copper/Cobalt sulfides on nickel foam as an enhanced 3D hierarchical catalyst to activate monopersulfate for Rhodamine b degradation. *J. Colloid Interf. Sci.* **2022**, *613*, 168–181. [CrossRef]
26. Jiang, L.P.; Wei, Z.Y.; Ding, Y.H.; Ma, Y.Y.; Fu, X.; Sun, J.; Ma, M.; Zhu, W.X.; Wang, J.L. In-situ synthesis of self-standing cobalt-doped nickel sulfide nanoarray as a recyclable and integrated catalyst for peroxymonosulfate activation. *Appl. Catal. B-Environ.* **2022**, *307*, 121184. [CrossRef]
27. Hu, L.M.; Zhang, G.S.; Liu, M.; Wang, Q.; Dong, S.Y.; Wang, P. Application of nickel foam-supported Co_3O_4-Bi_2O_3 as a heterogeneous catalyst for BPA removal by peroxymonosulfate activation. *Sci. Total Environ.* **2019**, *647*, 352–361. [CrossRef]
28. Liu, N.; Chen, X.Y.; Zhang, J.L.; Schwank, J.W. A review on TiO_2-based nanotubes synthesized via hydrothermal method: Formation mechanism, structure modification, and photocatalytic applications. *Catal Today* **2014**, *225*, 34–51. [CrossRef]
29. Guo, Y.G.; Lou, X.Y.; Fang, C.L.; Xiao, D.X.; Wang, Z.H.; Liu, J.S. Novel Photo-Sulfite System: Toward Simultaneous Transformations of Inorganic and Organic Pollutants. *Environ. Sci. Technol.* **2013**, *47*, 11174–11181. [CrossRef]
30. Wang, Y.R.; Tian, D.F.; Chu, W.; Li, M.R.; Lu, X.W. Nanoscaled magnetic $CuFe_2O_4$ as an activator of peroxymonosulfate for the degradation of antibiotics norfloxacin. *Sep. Purif. Technol.* **2019**, *212*, 536–544. [CrossRef]
31. Huang, Y.; Han, C.; Liu, Y.Q.; Nadagouda, M.N.; Machala, L.; O'Shea, K.E.; Sharma, V.K.; Dionysiou, D.D. Degradation of atrazine by $Zn_xCu_{1-x}Fe_2O_4$ nanomaterial-catalyzed sulfite under UV-vis light irradiation: Green strategy to generate $SO_4^{\cdot-}$. *Appl. Catal. B-Environ.* **2018**, *221*, 380–392. [CrossRef]
32. Li, Y.; Ma, S.; Xu, S.; Fu, H.; Li, Z.; Li, K.; Sheng, K.; Du, J.; Lu, X.; Li, X.; et al. Novel magnetic biochar as an activator for peroxymonosulfate to degrade bisphenol A: Emphasizing the synergistic effect between graphitized structure and $CoFe_2O_4$. *Chem. Eng. J.* **2020**, *387*, 124094. [CrossRef]
33. Dong, X.B.; Ren, B.X.; Sun, Z.M.; Li, C.Q.; Zhang, X.W.; Kong, M.H.; Zheng, S.L.; Dionysiou, D.D. Monodispersed $CuFe_2O_4$ nanoparticles anchored on natural kaolinite as highly efficient peroxymonosulfate catalyst for bisphenol A degradation. *Appl. Catal. B-Environ.* **2019**, *253*, 206–217. [CrossRef]
34. Fedorov, K.; Plata-Gryl, M.; Khan, J.A.; Boczkaj, G. Ultrasound-assisted heterogeneous activation of persulfate and peroxymonosulfate by asphaltenes for the degradation of BTEX in water. *J. Hazard. Mater.* **2020**, *397*, 122804. [CrossRef] [PubMed]
35. Guan, C.; Jiang, J.; Shen, Y.; Pang, S.; Luo, C.; Zhao, X. Carbon Materials Inhibit Formation of Nitrated Aromatic Products in Treatment of Phenolic Compounds by Thermal Activation of Peroxydisulfate in the Presence of Nitrite. *Environ. Sci. Technol.* **2019**, *53*, 9054–9062. [CrossRef] [PubMed]
36. Nie, C.; Dai, Z.; Meng, H.; Duan, X.; Qin, Y.; Zhou, Y.; Ao, Z.; Wang, S.; An, T. Peroxydisulfate activation by positively polarized carbocatalyst for enhanced removal of aqueous organic pollutants. *Water Res.* **2019**, *166*, 115043. [CrossRef] [PubMed]

37. Li, S.; Liu, C.; Lv, W.; Liu, G. Incorporating Oxygen Atoms in a SnS_2 Atomic Layer to Simultaneously Stabilize Atomic Hydrogen and Accelerate the Generation of Hydroxyl Radicals for Water Decontamination. *Environ. Sci. Technol.* **2022**, *56*, 4980–4987. [CrossRef] [PubMed]
38. Tan, C.Q.; Gao, N.Y.; Deng, Y.; Deng, J.; Zhou, S.Q.; Li, J.; Xin, X.Y. Radical induced degradation of acetaminophen with Fe_3O_4 magnetic nanoparticles as heterogeneous activator of peroxymonosulfate. *J. Hazard. Mater.* **2014**, *276*, 452–460. [CrossRef]
39. Chen, L.; Duan, J.; Du, P.H.; Sun, W.L.; Lai, B.; Liu, W. Accurate identification of radicals by in-situ electron paramagnetic resonance in ultraviolet-based homogenous advanced oxidation processes. *Water Res.* **2022**, *221*, 118747. [CrossRef]
40. Wen, Y.H.; Sharma, V.K.; Ma, X.M. Activation of Peroxymonosulfate by Phosphate and Carbonate for the Abatement of Atrazine: Roles of Radical and Nonradical Species. *ACS ES&T Wat.* **2022**, *2*, 635–643. [CrossRef]
41. Zhen, J.Y.; Zhang, S.S.; Zhuang, X.M.; Ahmad, S.; Lee, T.; Si, H.Y.; Cao, C.B.; Ni, S.Q. Sulfate radicals based heterogeneous peroxymonosulfate system catalyzed by CuO-Fe_3O_4-Biochar nanocomposite for bisphenol A degradation. *J. Water Process. Eng.* **2021**, *41*, 102078. [CrossRef]
42. Chai, H.; Yang, C.Y.; Xu, P.; Wang, P.; Qu, J.H.; Zhang, G.S. Enhanced visible-light photocatalytic activity with Fe_2O_3-ZnO@C/g-C_3N_4 heterojunction: Characterization, kinetics, and mechanisms. *J. Clean Prod.* **2022**, *377*, 134511. [CrossRef]
43. Guo, S.; Wang, H.J.; Yang, W.; Fida, H.; You, L.M.; Zhou, K. Scalable synthesis of Ca-doped α-Fe_2O_3 with abundant oxygen vacancies for enhanced degradation of organic pollutants through peroxymonosulfate activation. *Appl. Catal. B-Environ.* **2020**, *262*, 118250. [CrossRef]
44. Tan, L.; Yu, J.T.; Wang, H.Y.; Gao, H.T.; Liu, X.; Wang, L.; She, X.L.; Zhan, T.R. Controllable synthesis and phase-dependent catalytic performance of dual-phase nickel selenides on Ni foam for overall water splitting. *Appl. Catal. B-Environ.* **2022**, *303*, 120915. [CrossRef]
45. Hao, J.; Liu, J.; Wu, D.; Chen, M.; Liang, Y.; Wang, Q.; Wang, L.; Fu, X.-Z.; Luo, J.-L. In situ facile fabrication of $Ni(OH)_2$ nanosheet arrays for electrocatalytic co-production of formate and hydrogen from methanol in alkaline solution. *Appl. Catal. B-Environ.* **2021**, *281*, 119510. [CrossRef]
46. Zhu, J.; Zhu, Y.; Zhou, W. Cu-doped Ni-LDH with abundant oxygen vacancies for enhanced methyl 4-hydroxybenzoate degradation via peroxymonosulfate activation: Key role of superoxide radicals. *J. Colloid Interface Sci.* **2022**, *610*, 504–517. [CrossRef]
47. Liu, Y.; Guo, H.G.; Zhang, Y.L.; Tang, W.H.; Cheng, X.; Li, W. Heterogeneous activation of peroxymonosulfate by sillenite $Bi_{25}FeO_{40}$: Singlet oxygen generation and degradation for aquatic levofloxacin. *Chem. Eng. J.* **2018**, *343*, 128–137. [CrossRef]
48. Zhang, L.S.; Jiang, X.H.; Zhong, Z.A.; Tian, L.; Sun, Q.; Cui, Y.T.; Lu, X.; Zou, J.P.; Luo, S.L. Carbon Nitride Supported High-Loading Fe Single-Atom Catalyst for Activation of Peroxymonosulfate to Generate $^1O_2$ with 100 % Selectivity. *Angew. Chem.-Int. Edit.* **2021**, *60*, 21751–21755. [CrossRef]